Article

Structural change analysis of cerianite in weathered residual rare earth ore by mechanochemical reduction using x-ray absorption fine structure

Tatsuya Kato [1], Yuki Tsunazawa [2], Wenying Liu [3] and Chiharu Tokoro [4]*

[1] Graduate School of Creative Science and Engineering, Waseda University, 3-4-1 Okubo, Shinjuku-ku Tokyo, 169-8555, Japan; tatsuya.kato@aoni.waseda.jp
[2] National Institute of Advanced Industrial Science and Technology, 1-1-1 Higashi, Tsukuba, Ibaraki, 305-8567, Japan; tsunazawa-y@aist.go.jp
[3] Department of Materials Engineering, University of British Columbia, 309-6350 Stores Road, Vancouver, BC V6T 1Z4, Canada; wenying.liu@ubc.ca
[4] Faculty of Science and Engineering, Waseda University, 3-4-1 Okubo, Shinjuku-ku, Tokyo, 169-8555, Japan
* Correspondence: tokoro@waseda.jp; Tel.: +81-3-5286-3320

Abstract: Prolonged high-intensity grinding can modify the crystal structure of solid substances and/or induce chemical reaction, which is referred to as mechanochemical reaction. Such reactions can exert positive influences on hydrometallurgical processes, therefore, many researchers have applied mechanochemical reactions for metals dissolution from minerals. The mechanism of mechanochemical reaction has been investigated using solid analyses and simulations. Structural changes caused by mechanochemical reaction are not yet sufficiently clarified because the ground samples are amorphous. The objective of this study was to analyze structural changes of cerianite in weathered residual rare earth ore by mechanochemical reduction. Structural change was analyzed by x-ray absorption near-edge structure and extended x-ray absorption fine structure analysis at the cerium L_{III}- and K-edges. These analyses revealed that the structural change of cerianite in this ore induced by mechanochemical reduction involved oxygen vacancy production. The process of the oxygen vacancy formation was closely coupled with the quantum effect of localization–delocalization of the 4f electron of cerium.

Keywords: oxygen vacancy; extended x-ray absorption fine structure; high-intensity grinding; local structure; quantum effect

1. Introduction

Cerianite is tetravalent cerium dioxide (CeO_2) and has the fluorite structure (space group $(Fm\bar{3}m)$) [1]. In nature, cerianite exists in rare earth ores [2–5]. Cerianite has oxygen storage capacity due to a facile redox reaction from tetra- to trivalent cerium, as described in equation (1) [6], and the ability to improve dispersion of noble metals [7] and provide thermal stabilization of alumina supports [8]. Owing to these unique properties, cerianite has been widely used as a promoter of the three-way catalyst for automobile exhaust emission control [6, 7].

$$CeO_2 \rightarrow CeO_{2-x} + \frac{x}{2}O_2 \quad (1)$$

In addition, it has been reported that the reducibility of cerianite is enhanced by addition of yttrium [9, 10], gadolinium [11, 12], and zirconium to form a solid solution [13, 14]. Previous papers [9–14] reported that a solid solution of cerianite was reduced from tetra- to trivalent cerium at moderate temperatures (600–700 ℃), while pure cerianite reduced only at high temperature (<

1200 ℃) [15]. The reaction properties, such as structural changes and activation energy of solid solutions of cerianite, have been investigated using both experimental and simulation approaches. In the experimental approaches, X-ray diffraction analysis [16], electrical conductivity measurements [17], and X-ray absorption fine structure (XAFS) analysis [9–14] were usually used to investigate the reaction mechanism and structural changes induced by the addition of yttrium, gadolinium, and zirconium. In the simulation approaches, the activation energy for oxygen migration in a solid solution of cerianite was calculated, using structural change analysis based on XAFS [18, 19].

It is known that the redox reaction of cerianite, as described by equation (1), only occurs on heating above moderate temperatures; however, our previous paper [2] recently reported that this redox reaction of cerianite in a weathered residual rare earth ore also occurred by planetary ball milling at room temperature.

A reaction that occurs on grinding, such as this redox reaction, is generally known as a mechanochemical reaction [20, 21]. High-intensity grinding, like planetary ball milling, has the ability to modify crystal structures of solid substances and/or induce a chemical reaction, which is referred to as mechanochemical reaction. Mechanochemical reactions have a positive influence on hydrometallurgical processes and have been applied for metals dissolution from ores [2, 5, 20–24]; however, these studies only focused on investigation of the reaction mechanism. There is still limited knowledge of mechanochemical reactions and their theory has not been established. To apply mechanochemical reactions with high-intensity grinding to practical use in hydrometallurgical processes, it is strongly desired to establish the theory.

The objective of this study was to clarify the structural change of cerianite in a weathered residual rare earth ore during mechanochemical reduction. We performed grinding on the ore using a planetary ball mill. The ground samples were analyzed by XAFS at the cerium L_{III}- [2] and K-edges because that was amorphous and the concentration of cerium in the ore was much lower than that of other elements. We then performed extended x-ray absorption fine structure (EXAFS) analysis using XAFS spectra at the cerium K-edge to clarify the structural change of cerianite in the ore caused by the planetary ball milling.

2. Materials and Methods

2.1. Analytical sample

The weathered residual rare earth ore used in this study was obtained from the Republic of South Africa. Detailed characterizations were described in our previous paper [2]. Briefly, as shown in Tables 1 and 2, the major chemical composition of this ore was determined by x-ray fluorescence (XRF; ZSX PrimusIII+, Rigaku Corporation, Japan), while concentrations of the rare earth elements were analyzed by laser-ablation inductively coupled plasma mass spectrometry (LA–ICP–MS; 7500 Series, Agilent Technologies, USA). Mineral liberation analysis (MLA; QuantaF Co., FEI, USA) revealed that this ore contained four types of cerium minerals: britholite-(Ce) [$(Ce,Ca,Th,La,Nd)_5(SiO_4,PO_4)_3(OH,F)$], cerianite [$(Ce,Th)O_2$], cerite [$Ce_9Fe(SiO_4)_6[(SiO_3),(OH)](OH)_3$], and monazite-(Nd) [$(Nd,Ce,La)(P,Si)O_4$]. Of these, britholite-(Ce), cerite, and monazite-(Nd) were trivalent cerium minerals, while cerianite was the only tetravalent cerium mineral.

Grinding experiments using a planetary ball mill (PM100, Verder Scientific Co. Ltd., Japan) were performed under the same conditions as reported in our previous paper [2]. Briefly, each experiment employed 100 g ore; the rotation speed of the mill was fixed at 300 rpm; 25 chromium steel balls of 19 mm diameter were used as the grinding media. Grinding time was 10, 60 and 720 min. The specific surface areas of the samples, without and with grinding, as measured by a high-efficiency specific surface area and pore distribution analyzer (ASAP 2020 Series, Shimadzu, Japan), are shown in Table 3.

XAFS analysis at the cerium L_{III}-edge of samples without and with grinding was performed using the BL5S1 beamline at Aichi Synchrotron Radiation Center, Japan. XAFS spectra at the

cerium L_{III}-edge have an advantage in evaluating the oxidation state of cerium. The valence of cerium was evaluated using x-ray absorption near-edge structure (XANES) analysis in the range of 5720–5740 eV, using cerium fluoride (CeF_3) and tetravalent cerium oxide (CeO_2) as reference materials. The concentrations of tri- and tetravalent cerium in the samples without and with grinding are shown in Table 4, which was discussed in our previous paper [2].

Table 1. Chemical composition of weathered residual rare earth ore, as analyzed by x-ray fluorescence [mass %] [2]

SiO_2	Fe_2O_3	Al_2O_3	Na_2O	MgO	P_2O_5	K_2O	CaO	TiO_2	MnO	Others
68.6	16.2	7.3	0.3	0.4	0.3	2.1	0.2	0.3	0.2	4.1

Table 2. Concentrations of rare earth elements in weathered residual rare earth ore, as analyzed by laser-ablation inductively coupled plasma mass spectrometry [mg/dm^3] [2]

Sc	Y	La	Ce	Pr	Nd	Sm	Eu
5.3	1384.1	926.5	2495.5	236.8	903.3	200.0	11.2
Gd	Tb	Dy	Ho	Er	Tm	Yb	Lu
224.2	37.4	236.2	50.4	153.7	23.1	137.9	19.6

Table 3. Specific surface area of sample without and with grinding [m^2/g] [2]

Grinding time [min]	Specific surface area
0	16.2
10	23.8
60	19.1
720	10.4

Table 4. Concentrations of tri- and tetravalent cerium in samples without and with grinding, based on x-ray absorption near-edge structure analysis at the cerium L_{III}-edge [%] [2]

Grinding time [min]	Concentration of trivalent cerium	Concentration of tetravalent cerium
0	50.71	49.29
10	54.47	45.53
60	70.20	29.80
720	89.80	10.20

2.2. X-ray absorption fine structure analysis at cerium K-edge

XAFS analysis, including XANES and EXAFS, is a very powerful analytical technique for an amorphous sample. In particular, local structure in a specific atom can be analyzed using EXAFS. Low-to-medium-energy synchrotron facilities are relatively accessible, so most XAFS analysis for cerianite has been conducted at the cerium L_{III}-edge (5.7×10^3 eV) [25–27]. EXAFS analysis at the cerium L_{III}-edge has somewhat lower accuracy for derived structural parameters due to its limited data range, arising from the small energy separation between the L_{III}- and L_{II}-edges [25–27]. When XAFS analysis for cerianite was conducted at the cerium K-edge (4.0×10^4 eV), more accurate local structure around the cerium atom could be obtained because of the larger EXAFS data range, as described previously [28].

To analyze the structural change caused by grinding, XAFS analysis at the cerium K-edge was conducted on samples without and with grinding using the BL14B2 beamline at the SPring-8 Synchrotron Radiation Facility, Japan. All spectra were obtained at room temperature. The electron storage ring was operated at 8.0 GeV with a stored current of 99.6 mA. Energy was scanned from 40 290 eV to 41 233 eV using a step size of 6 eV. Continuous x-rays from synchrotron radiation were monochromatized using a silica (311) double-crystal monochromator. The XAFS

spectra for all samples were obtained in fluorescence mode using a 19-element germanium (Ge) solid-state detector. Cerium phosphate ($CePO_4$) and CeO_2 were used as reference materials.

The EXAFS functions were derived from the raw XAFS spectra by pre- and post-edge linear background subtraction and then normalized with respect to the edge jump. After being k^3-weighted, where k is the photoelectron wave number, the EXAFS function was Fourier transformed from the k^3-weighted EXAFS function to a radial distribution function (RDF) using a Hanning window function within 1–12 × 10^{10} m^{-1}. Structural parameters for different coordination shells surrounding both the central tri- and tetravalent cerium atoms, i.e., coordination number, atomic distance, and Debye–Waller factor, were obtained by curve fitting using both the k^3-weighted EXAFS function and RDF. Structural parameters were obtained from fitting the RDF in the interval of 1.5–4.0 × 10^{-10} m, using contributions from the first to fourth coordination shells (Ce(IV)–O, Ce(III)–O, Ce(III)–Ce(III), and Ce(IV)–Ce(IV)). The theoretical phases and amplitude functions for these shells were calculated using FEFF 6.0 software [29, 30]. All EXAFS analyses were performed using Athena and Artemis software [31].

3. Results and Discussion

3.1. X-ray absorption near-edge structure analysis

The XAFS spectra at the cerium K- and L_{III}-edges [2] corresponding to the XANES region are shown in Figure 1 for samples without and with grinding. Tri- and tetravalent cerium peaks at the cerium K-edge XAFS spectra were observed at 40 460 eV and 40 470 eV, respectively. The valence of cerium was already identified by XANES analysis at the cerium L_{III}-edge XAFS spectra, as shown in Table 4 [2]. The concentration of trivalent cerium significantly increased with grinding time. It was confirmed by both the cerium K- and L_{III}-edge XAFS spectra that the energetic shift corresponded to the change in valence of cerium (Figure 1(a)). The results of XANES analysis using XAFS spectra at the cerium K-edge are shown in Table 5. Compared with the data in Table 4, the trend, in which the concentration of trivalent cerium significantly increased with grinding time, was the same. These results showed that XAFS spectra at the cerium K-edge were sufficient to identify the valence of cerium in samples both without and with grinding [25, 26].

Cerium is the first element in the Periodic Table with a partially occuped f orbital: its arrangement of electrons is [Xe core]$4f^1$[Xe core]$5d^16s^2$ ($1s^22s^22p^63s^23p^63d^{10}4s^24p^64d^{10}4f^15s^25p^65d^16s^2$). From Figure 1(b), the XAFS spectra at the cerium L_{III}-edge of CeO_2 had two characteristic peaks at 5730 and 5737 eV, while that of CeF_3 had only one peak at 5725 eV. The peaks of CeO_2 at 5730 eV and 5737 eV are derived from the 2p to $(4f^1)5d$ electronic transition, which results from interactions between the cerium 4f electron and the nearest oxygen 2p electron, and from the 2p to $(4f^0)5d$ electronic transition, respectively [32, 33]. The peak of CeF_3 at 5725 eV is derived from the 2p to $(4f^1)5d$ electronic transition [32, 33]. In CeO_2, all tetravalent cerium normally leaves the host atoms and transfers into the 2p bands of two oxygen atoms; in trivalent cerium trioxide (Ce_2O_3), the cerium 4f electron is fully localized [34]. From the above discussion, it is suggested that the structural change of cerianite in weathered residual rare earth ore during mechanochemical reduction involved localication–delocalization of the cerium 4f electron.

Table 5. Concentrations of tri- and tetravalent cerium in samples without and with grinding, based on x-ray absorption near-edge structure analysis at cerium K-edge [%]

Grinding time [min]	Concentration of trivalent cerium	Concentration of tetravalent cerium
0	30.46	69.55
10	31.92	68.08
60	50.01	49.99
720	74.38	25.62

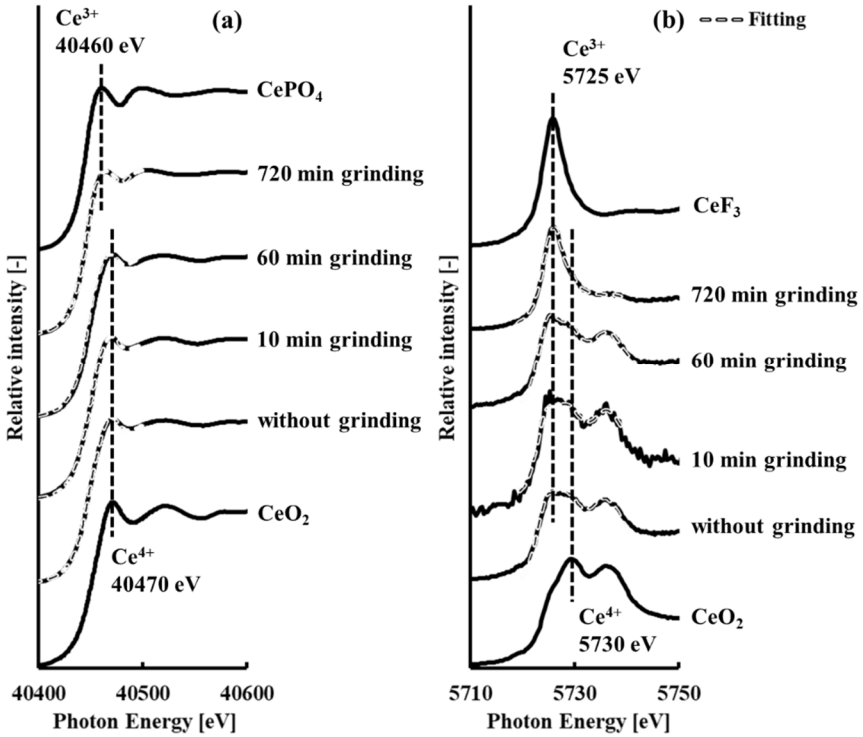

Figure 1. Cerium (a) K- and (b) L_{III}-edge x-ray absorption fine structure spectra [2] corresponding to x-ray absorption near the edge structure region of samples without and with grinding, showing resolved components of tri- and tetravalent cerium based on cerium fluoride or cerium phosphate and tetravalent cerium oxide reference spectra, respectively.

3.2. Extended x-ray absorption fine structure analysis

The k^3-weighted EXAFS spectra and RDF of CeO_2 of samples without and with grinding are shown in Figures 2 and 3, respectively. The curve-fitted results are plotted and the corresponding parametric values are listed in Table 6. It should be noted that the third shell (Ce(III)–Ce(III)) contribution was quite minor relative to that of the fourth shell (Ce(IV)–Ce(IV)), and significant overlap existed between these two shells in the RDF.

Figure 2 shows that the k^3-weighted EXAFS spectra of the sample without grinding was similar to that of the sample ground for 10 min, but these differed from those of samples ground for 60 min and 720 min. This trend is also shown in the RDF (Figure 3). These results clearly showed that the structure of cerianite in the weathered residual rare earth ore started to change after 10 min of grinding.

The curve-fitting results in Table 6 show that the coordination numbers of Ce(IV)–O and Ce(IV)–Ce(IV) in the cerianite decreased as grinding time increased, while those of Ce(III)–O and Ce(III)–Ce(III) increased. From the above discussion, the results of EXAFS analysis suggested that the structure of the ore changed from cerianite to Ce_2O_3 because of a mechanochemical reduction [2]. Cerianite has the fluorite structure (space group ($Fm\bar{3}m$)) [1] (Figure 4(a)). Skorodumova et al. reported that the C-type structure of Ce_2O_3 (space group ($Ia\bar{3}$)) was produced on completion of the reduction process [34–36] (Figure 4(b)). This structure (Figure 4(b)) can be constructed from eight unit cells of cerianite (Figure 4(a)) with 25 % oxygen vacancies ordered in a particular way [34]. The structure change from cerianite to the C-type structure of Ce_2O_3 involves minimal reorganization of the skeleton arrangement of the cerium atoms [34]. This structural property should facilitate the excellent reversibility of the reduction–oxidation process.

The atomic distances of both Ce(IV)–O and Ce(III)–O in cerianite also decreased as grinding time increased, as shown in Table 6. This trend was similar to the case of Gd_2O_3-doped cerianite

[11]: Ohashi et al. reported that when gadolinium was doped at 30 % in cerianite, the Ce(IV)–O and Gd(III)–O atomic distances decreased by 0.032×10^{-10} m and 0.024×10^{-10} m, respectively [11]. Compared with this result, the decrease of atomic distance in the present system was large; thus, the decrease of atomic distances of Ce(IV)–O and Ce(III)–O in the cerianite represented significant structural changes.

The decreases of the Ce(IV)–O and Ce(III)–O atomic distances in the cerianite showed that oxygen vacancies occurred in the structure on grinding, and that oxygen ions surrounding these vacancies around both tri- and tetravalent cerium ions relaxed toward their adjacent vacancies [19]. Skorodumova et al. reported that it required 4.4×10^{2} kJ/mol to form an oxygen vacancy in pure cerianite, based on the full-potential linear muffin tin orbitals generalized gradient approximation (FP–LMTO–GGA) [34, 37, 38]. In our experimental system, it is suggested that this energy was mainly provided by the planetary ball milling. In addition, it is suggested that the distribution of oxygen vacancies in the stucture of cerianite is related to the valences and ionic radii of tri- and tetravalent cerium ions. In this system, the ionic radii of eight-coordinated tri- and tetravalent cerium are 1.143×10^{-10} m and 0.97×10^{-10} m, respectively [39]. These ionic radii are relatively similar, so oxygen vacancies are considered to be favored near trivalent cerium ions to ensure electrical neutrality. Indeed, Skorodumova et al. reported that it required only 25 kJ/mol, which was the lowest energy among positions that could form an oxygen vacancy, to form an oxygen vacancy adjacent to trivalent cerium in pure cerianite [34].

Formation of a cluster composed of oxygen vacancies and trivalent cerium ions has been proposed by some researchers, using the cluster model for the structure of cerianite, which is specified by the number of oxygen vacancies and their configuration and those of cations around the vacancies [11, 18, 19]. According to the cluster model, two models expressing the local structures around oxygen vacancies are proposed, as shown in Figure 5: one oxygen vacancy in the structure of cerianite is introduced for every two trivalent cerium ions, as required by the electroneutrality condition. In the type A model, one unit cell of cerianite contains one trivalent cerium and one oxygen vacancy, while the other unit cell contains one trivalent cerium and no oxygen vacancy; in the type B model, one unit cell of cerianite contains two trivalent ceriums and one oxygen vacancy. If only type A were formed, the Ce(III)–O atomic distance in the cerianite would not be expected to decrease as the concentration of trivalent cerium in the ore increased with grinding time; if only type B were formed, a similar trend would occur. If both types A and B co-existed, and the proportion of type A decreased and that of type B increased with grinding, then the Ce(III)–O atomic distance in the cerianite would decrease as the concentration of trivalent cerium in the ore increased with grinding time. From the above discussion, it is suggested that oxygen vacancies occurred in the cerianite in the weathered residual rare earth ore and changed the structure from that of fluorite to one in which types A and B co-existed and the proportion of type B increased as grinding time by planetary ball milling increased.

From the results of XANES and EXAFS analysis, it is suggested that the process of oxygen vacancy formation was closely coupled with the quantum effect of localization–delocalization of the 4f electron of cerium. Oxygen in cerianite has two extra electrons in the p band, provided by tetravalent cerium. When an oxygen vacancy is produced in cerianite, it is suggested that these two electrons are left behind and occupy the lowest possible empty state, which is the f band of cerium. Thus, tetravalent cerium in the cerianite is reduced to trivalent cerium (Figure 6).

Preprints (www.preprints.org) | NOT PEER-REVIEWED | Posted: 13 April 2019 doi:10.20944/preprints201904.0154.v1

Peer-reviewed version available at Minerals 2019, 9, 267; doi:10.3390/min9050267

Table 6. Cerium fitting results of radial distribution function for samples without and with grinding, assuming four kinds of cerium shells for tetravalent cerium oxide .

Sample	Shell	CN	R [×m^{-10}]	σ^2 [×m^{-20}]	ΔE$_0$
CeO_2	Ce(IV)-O	7.7	2.35	0.009	-10.3
	Ce(III)-O		-		
	Ce(III)-Ce(III)		-		
	Ce(IV)-Ce(IV)	12.2	3.84	0.005	
Without grinding	Ce(IV)-O	8.7	2.35	0.02	-9.3
	Ce(III)-O	0.2	2.46	0.04	
	Ce(III)-Ce(III)	0.3	3.81	0.002	
	Ce(IV)-Ce(IV)	12.1	3.83	0.008	
10 min grinding	Ce(IV)-O	8.0	2.36	0.02	-10.6
	Ce(III)-O	0.06	2.47	-0.01	
	Ce(III)-Ce(III)	0.2	3.81	0.001	
	Ce(IV)-Ce(IV)	11.4	3.84	0.008	
60 min grinding	Ce(IV)-O	4.0	2.31	0.006	2.4
	Ce(III)-O	3.9	2.42	0.02	
	Ce(III)-Ce(III)	7.4	3.77	0.008	
	Ce(IV)-Ce(IV)	5.4	3.79	0.009	
720 min grinding	Ce(IV)-O	0.1	2.30	0.009	-3.4
	Ce(III)-O	8.4	2.42	0.03	
	Ce(III)-Ce(III)	10.0	3.76	0.04	
	Ce(IV)-Ce(IV)	2.6	3.79	0.0009	

CN: coordination number; R [×m^{-10}]: atomic distance; ΔE_0: threshold E_0 shift; σ^2 [×m^{-20}]: Debye–Waller factor

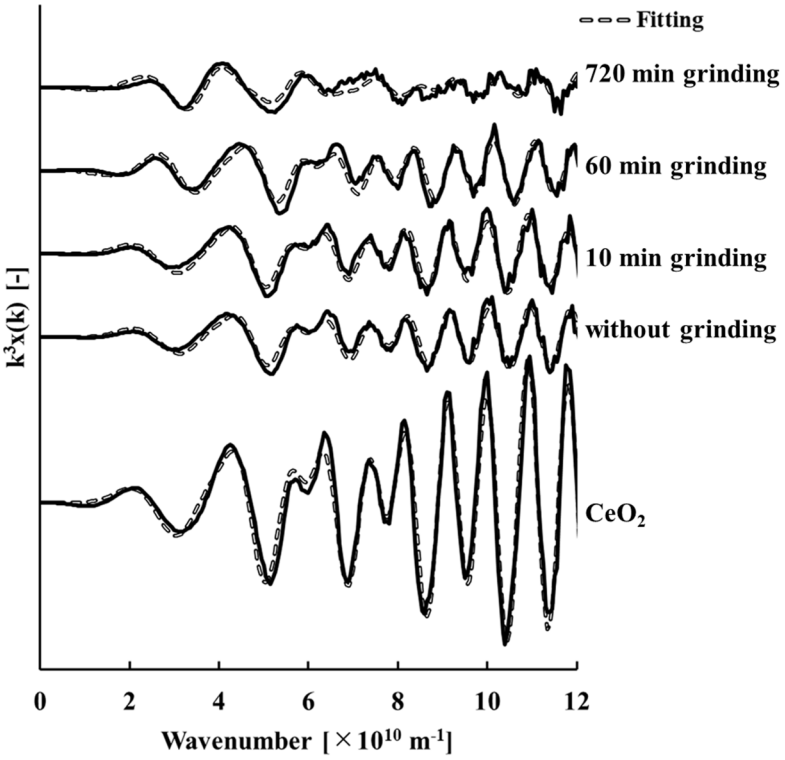

Figure 2. k^3-weighted cerium K-edge extended x-ray absorption fine structure spectra of tetravalent cerium oxide for samples without and with grinding.

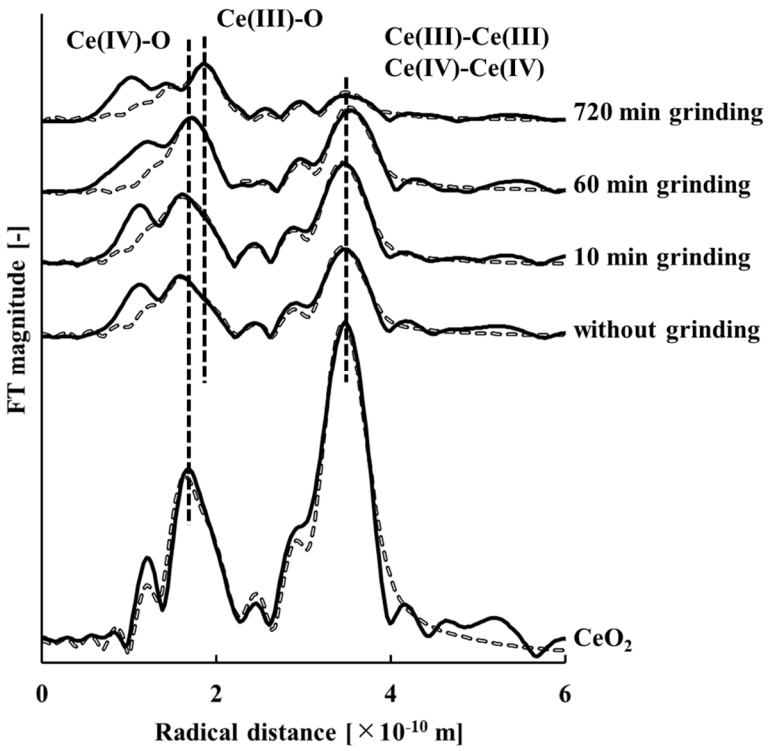

244 **Figure 3.** Radial distribution functions of tetravalent cerium oxide for samples without and with
245 grinding.

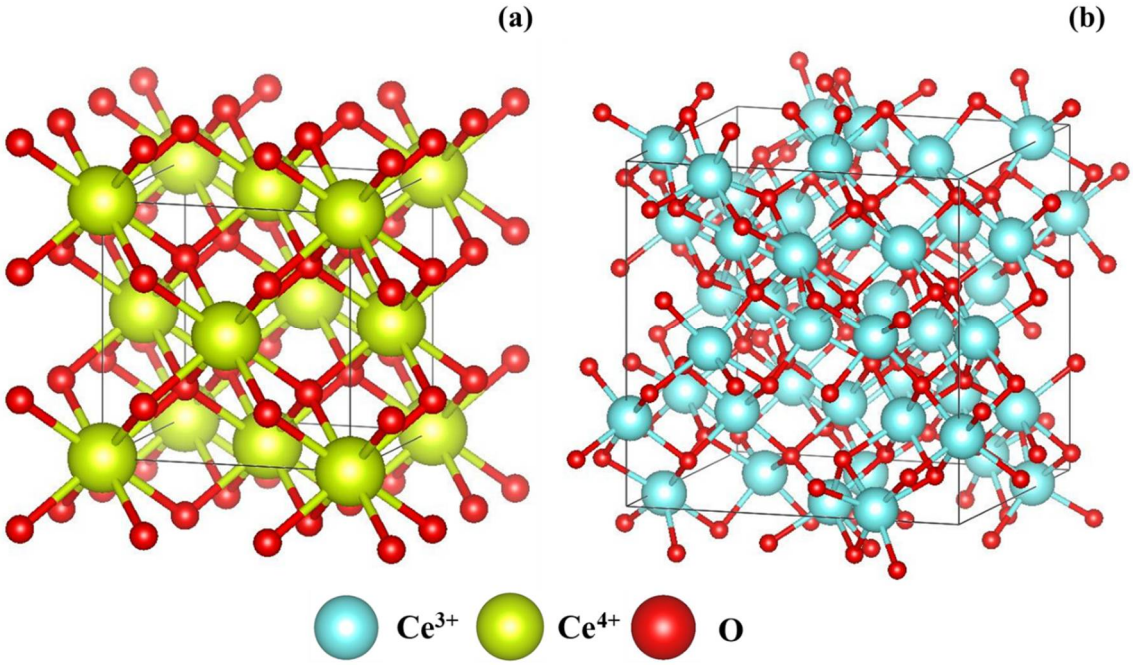

246 **Figure 4.** Lattice unit cells for (a) tetravalent cerium oxide and (b) C-type structure of trivalent cerium
247 trioxide [40].

Peer-reviewed version available at Minerals 2019, 9, 267; doi:10.3390/min9050267

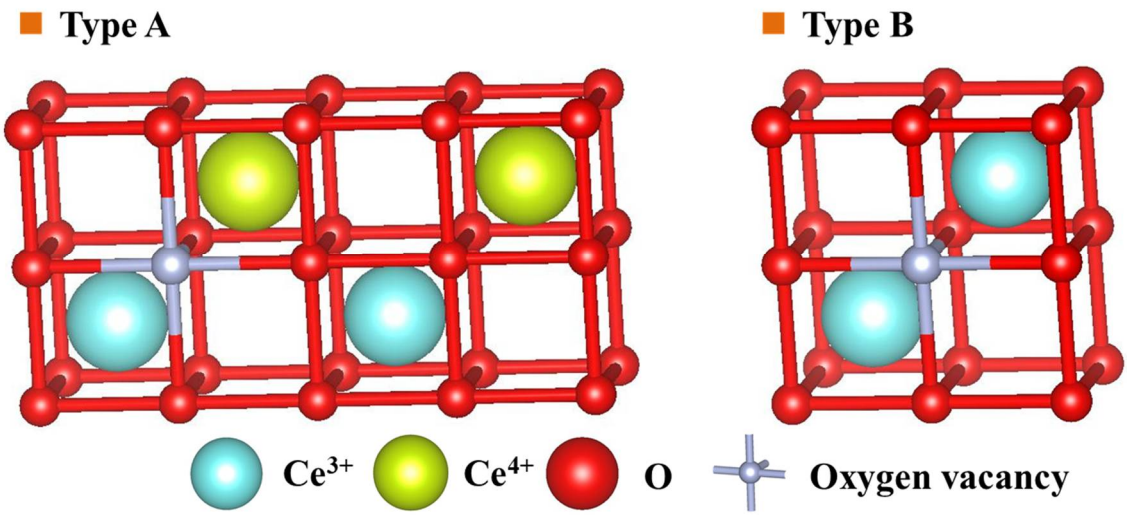

Figure 5. Two models expressing the local structure around oxygen vacancies in tetravalent cerium oxide [40].

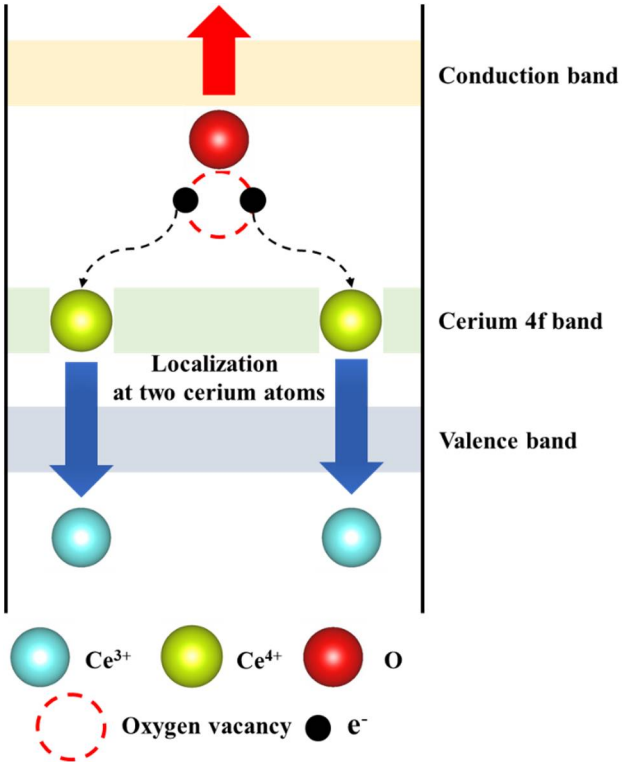

Figure 6. Schematic process of oxygen vacancy formation in tetravalent cerium oxide.

4. Conclusions

The objective of this study was to clarify the structural change of cerianite in weathered residual rare earth ore during mechanochemical reduction. Results of XANES and EXAFS analysis revealed that the structural change involved oxygen vacancies produced in the cerianite. The process of the oxygen vacancy formation was closely coupled with the quantum effect of localization–delocalization of the 4f electron of cerium. EXAFS analysis showed that the atomic distances of both Ce(III)–O and Ce(IV)–O decreased, which indicated that the cerianite changed from the fluorite structure to one in which types A and B co-existed and the proportion of type B increased as grinding time by planetary ball milling increased.

Author Contributions: Conceptualization, C.T., W.L. and T. K.; formal analysis, T.K.; investigation, T.K. and Y.T.; resources, Y.T.; writing—original draft preparation, T.K.; writing—review and editing, Y.T., W.L. and C.T.; supervision, C.T.; project administration, C.T.; funding acquisition, C.T.

Funding: This study was partially supported by the Hosokawa Powder Technology Foundation, under Grant Nos. 18504 and 2018, and the Joint Research Center for Environmentally Conscious Technologies in Materials Science (Project No. 30006) at ZAIKEN, Waseda University.

Acknowledgments: The synchrotron radiation experiments were performed using a BL5S1 beamline courtesy of the Aichi Synchrotron Radiation Center, Aichi Science & Technology Foundation, Aichi, Japan (Proposal No. 201801021), and BL14B2 beamline of SPring-8, with approval of the Japan Synchrotron Radiation Research Institute (Proposal No. 2018A1696, 2019A1777). Part of this work was performed as a component of the activities of the Research Institute of the Sustainable Future Society, Waseda Research Institute for Science and Engineering, Waseda University, and the Joint Usage/Research Center on Joining and Welding, Osaka University. We thank Kathryn Sole, PhD, from Edanz Group (www.edanzediting.com/ac) for editing a draft of this manuscript.

Conflicts of Interest: The authors declare no conflict of interest.

References

1. Trovarelli, A.; Fornasiero, P. *Catalysis by ceria and related materials*, 2nd ed.; Imperial College Press: London, United Kingdom of Great Britain and Northern Ireland, 2013; pp. 1 – 881.
2. Kato, T.; Granata, G.; Tsunazawa, Y.; Takagi, T.; Tokoro, C. Mechanism and kinetics of enhancement of cerium dissolution from weathered residual rare earth ore by planetary ball milling. *Minerals Engineering* **2019**, *134*, 365 - 371.
3. Bochevslaya, Y. G.; Abisheva, Z. S.; Karshigina, Z. B.; Sargelova, E. A.; Kvyatkovskaya, M. N.; Akchulakova, S. T. Effect of the temperature conditions of sulfation process on extraction of rare earth metals from refractory ore. *Metallurgist* **2018**, *62*, 574 – 586.
4. Peretyazhko, I. S.; Savina, E. A.; Karmanov, N. S.; Dmitrieva, A. S. Immiscibility of fluoride – calcium and silicate melts in trachyrhyolitic magma: data on acidic volcanic rocks from the nyalga basin, central mongolia. *Petrologiya* **2018**, *26(4)*, 400 – 425.
5. Kato, T.; Granata, G.; Tokoro, C. Evaluation of acids onto the light rare earth elements dissolution from weathered residual rare earth ore activated by mechanochemical treatment by grinding. *Journal of the Society of Powder Technology, Japan* **2019**, in press.
6. Yao, H. C.; Yao, Y. F. Y. Ceria in automotive exhaust catalysts: I. oxygen storage. *Journal of Catalysis* **1984**, *86*, 254 – 265.
7. Diwell, A. F.; Rajaram, R. R.; Shaw, H. A.; Truex, T. J. The role of ceria in three-way catalysts. *Studies in Surface Science and Catalysis* **1991**, *71*, 139 – 152.
8. Harrison, B.; Diwell, A. F.; Hallett, C. Promoting platinum metals by ceria. *Platinum Metals Review* **1988**, *32(2)*, 73 – 83.
9. Wang, D. Y.; Nowick, A. S. Dielectric relaxation from a network of charged defects in dilute CeO_2:Y_2O_3 solid solutions. *Solid State Ionics* **1981**, *5*, 551 – 554.
10. Wang, D. Y.; Park, D. S.; Griffith, J.; Nowick, A. S. Oxygen-ion conductivity and defect interactions in yttria-doped ceria. *Solid State Ionics* **1981**, *2*, 95 – 105.
11. Ohashi, T.; Yamazaki, S.; Tokunaga, T.; Arita, Y.; Matsui, T.; Harami, T.; Kobayashi, K. EXAFS study of $Ce_{1-x}Gd_xO_{2-x/2}$. *Solid State Ionics* **1998**, *113 – 115*, 559 – 564.
12. Deguchi, H.; Yoshida, H.; Inagaki, T.; Horiuchi, M. EXAFS study of doped ceria using multiple data set fit. *Solid State Ionics* **2005**, *176*, 1817 – 1825.
13. Nagai, Y.; Yamamoto, T.; Tanaka, T.; Yoshida, S.; Nonaka, T.; Okamoto, T.; Suda, A.; Sugiura, M. X-ray absorption fine structure analysis of local structure of CeO_2-ZrO_2 mixed oxides with the same composition ratio (Ce/Zr = 1). *Catalysis Today* **2002**, *74*, 225 – 234.
14. Kaspar, J.; Fornasiero, P.; Balducci, G.; Monte, R. D.; Hickey, N.; Sergo, V. Effect of ZrO_2 content on textural and structural properties of CeO_2-ZrO_2 solid solutions made by citrate complexation route. *Inorganica Chimica Acta* **2003**, *349*, 217 – 226.
15. Bulfin, B.; Lowe, A. J.; Keogh, K. A.; Murphy, B. E.; Lubben, O.; Krasnikov, S. A.; Shvets, I. V. Analytical model of CeO_2 oxidation and reduction. *The Journal of Physical Chemistry C* **2013**, *117*, 24129 – 24137.

16. Meriani, S.; Spinolo, G. Powder data for metastable $Zr_xCe_{1-x}O_2$ (x = 0.84 to 0.40) solid solutions with tetragonal symmetry. *Powder Diffraction* **1987**, *2(4)*, 255 – 256.
17. Reidy, R. F.; Simkovich, G. Electrical conductivity and point defect behavior in ceria-stabilized zirconia. *Solid State Ionics* **1993**, *62*, 85 – 97.
18. Balducci, G.; Islam, M. S.; Kaspar, J.; Fornasiero, P.; Graziani, M. Bulk reduction and oxygen migration in the ceria-based oxides. *Chemistry of Materials* **2000**, *12*, 677 – 681.
19. Badlducci, G.; Kaspar, J.; Fornasiero, P.; Graziani, M.; Islam, M. S.; Gale, J. D. Computer simulations studies of bulk reduction and oxygen migration in CeO_2-ZrO_2 solid solutions. *The Journal of Physical Chemistry* **1997**, *101*, 1750 – 1753.
20. Pourghahramani, P.; Akhgar, B. N. Characterization of structural changes of mechanically activated natural pyrite using XRD line profile analysis. *International Journal of Mineral Processing* **2015**, *134*, 23 – 28.
21. Kahrizsangi, R. E.; Abbasi, M. H.; Saidi, A. Mechanochemical effects on the molybdenite roasting kinetics. *Chemical Engineering Journal* **2006**, *121*, 65 – 71.
22. Granata, G.; Takahashi, K.; Kato, T.; Tokoro, C. Mechanochemical activation of chalcopyrite: relationship between activation mechanism and leaching enhancement. *Minerals Engineering* **2019**, *131*, 280 – 285.
23. Minagawa, M.; Hisatomi, S.; Kato, T.; Granata, G.; Tokoro, C. Enhancement of copper dissolution by mechanochemical activation of copper ores: correlation between leaching experiments and DEM simulations. *Advanced Powder Technology* **2018**, *29*, 471 – 478.
24. Mitani, Y.; Tsunazawa, Y.; Okura, T.; Tokoro, C. Enhancement of copper leaching from chalcopyrite using wet-type ball mill. *Journal of the Society of Powder Technology, Japan* **2015**, 52, 723 - 729.
25. Nakada, R.; Tanaka, M.; Tanimizu, M.; Takahashi, Y. Aqueous speciation is likely to control the stable isotopic fractionation of cerium at varying pH. *Geochimica et Cosmochimica Acta* **2017**, *218*, 273 – 290.
26. Okamoto, Y.; Osugi, T.; Akabori, M.; Kobayashi, T.; Shiwaku, H. Chemical state analysis of high-temperature molten slag components by using high-energy XAFS. *Journal of Molecular Liquids* **2017**, *232*, 285 – 289.
27. Kumar, S.; Gautam, S.; Song, T. K.; Chae, K. H.; Jang, K. W.; Kim, S. S. Electronic structure study of Co doped CeO_2 nanoparticles using x-ray absorption fine structure spectroscopy. *Journal of Alloys and Compounds* **2014**, *611*, 329 – 334.
28. Rygel, J. L.; Chen, Y.; Pantano, C. G.; Shibata, T.; Du, J.; Kokou, L.; Woodman, R.; Belcher,J. Local structure of cerium in aluminophosphate and silicophosphate glasses. *Journal of the American Ceramic Society* **2011**, *94(8)*, 2442 – 2451.
29. Rehr, J. J.; Albers, R. C.; Zabinsky, S. I. High-order multiple-scattering calculations of x-ray-absorption fine structure. *Physical Review Letters* **1992**, *69*, 3399 – 3400.
30. Rehr, J. J. Recent developments in multiple-scattering calculations of XAFS and XANES. *Japanese Journal of Applied Physics* **1993**, *32(2)*, 8 – 12.
31. Ravel, B.; Newville, M. Athena, artemis, hephaestus: data analysis for x-ray absorption spectroscopy using IFEFFIT. *Journal of Synchrotron Radiation* **2005**, *12*, 537 -541.
32. Bianconi, A.; Marcelli, A.; Dexpert. H.; Karnatak, R.; Kotani, A.; Jo, T. Specific intermediate-valence state of insulating 4f compounds detected by L_3 x-ray absorption. *Physical Review B* **1987**, 35(2), 806 – 812.
33. Kaindl, G.; Schmiester, G.; Sampathkumaran, E. V. Pressure-induced changes in L_{III} x-ray-absorption near-edge structure of CeO2 and CeF4: relevance to 4f-electronic structure. *Physical Review B* **1988**, 38(14), 10174 – 10177.
34. Skorodumova, N. V.; Simak, S. L.; Lundqvist, B. L.; Abrikosov, L. A; Johansson, B. Quantum origin of the oxygen storage capability of ceria. *Physical Review Letters* **2002**, 89(16), 166601/1 – 166601/4.
35. Silva, J. L. F. D. Stability of the Ce_2O_3 phases: a DFT + U investigation. *Physical Review B* **2007**, 76(19), 193108-1 – 193108-4.
36. Bartos, A.; Lieb, K. P.; Uhrmacher, M.; Wiarda, D. Refinement of atomic positions in bixbyite oxide using perturbed angular correlation spectroscopy. *Acta Crystallographica Section B* **1993**, 49, 165 – 169.
37. Wills, J. M.; Johansson, B.; Eriksson, O. *Full-potential LMTO total energy and force calculations*, 1st ed.; Springer Verlag: Berlin, Federal Republic of Germany, 2000; pp. 1 – 148.

38. Perdew, J. P.; Chevary, J. A.; Vosko, S. H.; Jackson, K. A.; Pederson, M. R.; Singh, D. J.; Fiolhais, C. Atoms, molecule, solids, and surfaces: applications of the generalized gradient approximation for exchange and correlation. *Physical Review B* **1993**, 46(11), 6671 – 6687.
39. Shannon, R. D. Revised effective ionic radii and systematic studies of interatomic distances in halides and chalcogenides. *Acta Crystallogr* **1976**, *A32*, 751 – 767.
40. Momma, K.; Izumi, F. VESTA 3 for three-dimensional visualization of crystal, volumetric and morphology data. *Journal of Applied Crystallography* **2011**, 44, 1272 – 1276.